ENGINEERING

Characteristic boundaries associated with three-dimensional twins in hexagonal metals

Shujuan Wang[1], Mingyu Gong[1,2], Rodney J. McCabe[1]*, Laurent Capolungo[1], Jian Wang[2], Carlos N. Tomé[1]

Twinning is a critically important deformation mode in hexagonal close-packed metals. Twins are three-dimensional (3D) domains, whose growth is mediated by the motion of facets bounding the 3D twin domains and influences work hardening in metals. An understanding of twin transformations therefore necessitates that the atomic-scale structure and intrinsic mobilities of facets be known and characterized. The present work addresses the former point by systematically characterizing the boundary structures of 3D {$\bar{1}$012} twins in magnesium using high-resolution transmission electron microscopy (HRTEM). Eight characteristic facets associated with twin boundaries are reported, five of which have never been experimentally observed before. Further, molecular dynamics simulations suggest that the formation and motion of these facets is associated with the accumulation of twinning dislocations. This work provides insights into understanding the structural character of 3D twins and serves to develop strategies for modulating twin kinetics by modifying twin boundaries, such as solute segregation.

INTRODUCTION

Twinning is a major plastic deformation mechanism accommodating shear in hexagonal close packed (hcp) and other lower symmetry metals (i.e., Mg, Ti, Zr, Be, Sn, and U) (*1*–*3*), as well as in some high-performance steels (*4*, *5*) and in many cubic metals during high rate/stress loading (*6*, *7*). Twin domains are inherently three-dimensional (3D) defects, and the atomic-scale structure and intrinsic mobilities of twin boundaries, i.e., facets bounding the twin domains, condition the kinetics of twinning (*8*–*13*). Twin growth (as well as detwinning) is mediated by the nucleation and propagation of twinning dislocations (TDs) on facets bounding twin domains. This mechanism has been discussed in a series of recent atomistic simulation studies focused on the migration of two such facets: the coherent twin boundary (CTB) and basal-prismatic (BP/PB) (*11*–*16*). It has been recently shown that TDs and steps/facets are favorable sites for segregating impurities and alloying elements (*14*, *17*–*19*). These are found to either impede or facilitate twin migration. Our understanding of the kinetics of twinning and eventually our ability to modulate the transformation—possibly via the addition of solutes—are limited by our fundamental knowledge of the geometry, atomic-scale structure, and intrinsic mobility of the facets bounding twin domains. While there have been decades of work dedicated to understanding how dislocation core structures and mobility vary depending on their character (i.e., edge, screw, mixed, jogged, and kinked) (*20*–*23*) and on the materials chemistry, similar studies are only incipient in the case of twin facets.

Specifically, while twin domains are necessarily bound by numerous facets each with distinct geometry and structure, previous experimental studies have defined the twin boundary structure only from a single direction and thus elucidate only a single "boundary character." This would be akin to having an understanding of dislocation-mediated plasticity limited to considerations of only one dislocation character.

The most commonly activated twin mode in hcp metals is the {$\bar{1}$012} twin, defined by the K_1 = {$\bar{1}$012} twinning plane and the η_1 = <10$\bar{1}$1> twinning shear direction (*7*). A CTB is defined when the physical (habit) plane separating parent and twin is parallel to the K_1 plane common to both the twin and parent. At the micrometer scale, however, twin boundaries generally deviate significantly from the CTB relationship (*16*, *24*–*26*). Experimentally, the atomic-scale defects defining twin boundaries have only been definitively characterized along a single crystallographic direction, the <1$\bar{2}$10>, λ, that lies in the K_1 plane and is perpendicular to η_1 (*8*, *11*, *16*, *25*–*29*). These studies reveal a 2D perspective where twin boundaries are composed of CTBs and BP/PB facets with K_2/K_2 facets observed at some twin tips (*27*–*29*). BP/PB facets closely align (0001) and (10$\bar{1}$0) planes in the twin and parent, respectively, and K_2 facets closely align the {$\bar{1}$01$\bar{2}$} ‖ {$\bar{1}$01$\bar{2}$} K_2 planes in the twin and parent. We show examples of these facets in Results and Discussion. There is only one previous experimental study at the atomic scale of a {$\bar{1}$012} twin boundary viewed along a different direction, the <10$\bar{1}$1>, η_1 (*30*). The atomic structure of the twin boundary was not observed in the latter study because of the lack of contrast for an extended twin boundary along this zone axis. The study relied on complementary molecular dynamics (MD) simulations to suggest the serrated boundary to be composed of CTBs and semicoherent twist prismatic-prismatic (Twist-Pr2Pr2) facets with {$\bar{2}$110} ‖ {2$\bar{1}\bar{1}$0}. Critically, these facets were not directly observed experimentally.

Except for the classic studies from the <1$\bar{2}$10> direction and the single study along the <10$\bar{1}$1> direction, there have been no other atomic-scale studies describing {$\bar{1}$012} twin boundaries along other directions. Considering that twin growth takes place in 3D, there is a fundamental need for elucidating the propagation of twin interfaces in 3D, to which the studies from the <1$\bar{2}$10> direction provide only a partial answer. Here, we tackle the first and essential step in such a quest, namely, figuring out what are the facets that bound twin domains and their atomic configurations. We have undertaken the experimental atomic-scale characterization of the most common twin in hcp metals from six crystallographic directions and have found evidence of eight different boundary facets, five of which have never been experimentally observed. MD simulations further suggest

[1]Material Science and Technology Division, Los Alamos National Lab, Los Alamos, NM 87545, USA. [2]Mechanical and Materials Engineering, University of Nebraska-Lincoln, Lincoln, NE 68583, USA.
*Corresponding author. Email: rmccabe@lanl.gov

that the formation and motion of these facets are associated with the accumulation of TDs.

RESULTS AND DISCUSSION

Atomic-scale 3D characterization of {$\bar{1}$012} twin boundary facets

The 3D faceted structures of twin boundaries that are the basic elements for building arbitrary 3D twin shapes are characterized by analyzing many twins using atomic-scale high-resolution transmission electron microscopy (HRTEM) imaged along several different crystallographic directions, i.e., zone axes. Atomic-scale imaging of facets in TEM foils requires specific imaging conditions related to the foil normal, facet geometry, and crystallography. To image identifiable facets at the atomic scale, three conditions must be simultaneously satisfied. First, the viewing direction of both the twin and its parent must be along a low-index crystallographic direction, or zone axis, contained within the twinning plane rather than random directions. The crystallographic observation directions depend on the atomic configuration of the twinning plane, which is shown in Fig. 1A. The six lowest index zone axes in the twinning plane are as follows: <1$\bar{2}$10>, <2$\bar{2}$01>, <5$\bar{4}\bar{1}$3>, <3$\bar{2}\bar{1}$2>, <4$\bar{2}\bar{2}$3>, and <10$\bar{1}$1>. While the four-index Miller-Bravais indices for the observation directions seem high, the three-index Miller index equivalents are low, with <5$\bar{4}\bar{1}$3> and <4$\bar{2}\bar{2}$3> being <2$\bar{1}$1> and <201>, respectively. Second, because of the tilt limitation of the TEM holder, the deviation angle between the imaging direction and the normal direction of the TEM foil must be within the tilt range (<30°). We performed electron backscattered diffraction (EBSD) analysis on twin-jet polished TEM foils to preselect twins with proper orientations. Generally, each selected twin can be imaged along one low-index zone axis. Third, only edge-on facet planes relative to the imaging crystallographic direction can be identified from an HRTEM image. In many cases, twin facets in a TEM foil are inclined relative to the imaging direction resulting in a twin boundary with a diffuse appearance, and it is not possible to define the facets from the specific imaging condition. There is an experimental analogy between HRTEM imaging of twin facets and dislocation cores. One cannot image a dislocation core unless one is looking down the line direction of the dislocation, and the strain associated with a pure screw dislocation makes it difficult to image the atomic structure of the core. Similarly, not all twin boundary facets in our images are at ideal configurations for atomic-scale imaging. We report only the twin facets that are identifiable for the given TEM foil and imaging conditions.

The facets identified in this work were obtained from more than 30 individual twins (both extended boundaries and twin tips) preselected from hundreds of twins. Here, we use the term twin tip to describe the outer rim of a twin as viewed from a single zone axis. AQ3 Boundaries with large edge-on facets were observed along the <1$\bar{2}$10>, <5$\bar{4}\bar{1}$3>, <4$\bar{2}\bar{2}$3>, and <10$\bar{1}$1> zone axes, while no facets were observed along the <2$\bar{2}$01> and <3$\bar{2}\bar{1}$2> zone axes. Attempts were made to perform HRTEM at higher index zone axes, but none of the higher index zone axes showed facets and, in addition, gave relatively poor HRTEM imaging conditions. Figure 1B schematically depicts the observation zone axes and all of the observed facets. A 3D twin domain with an arbitrary shape could be formed by combining the basic elements of CTBs and these facets in different length/height ratios.

For the identification of facets, two steps were generally performed. First, we analyzed the potential interfaces according to the twin orientation relationship between matrix and twin along each zone axis. The planes in matrix and twin comprising an interface should be parallel or nearly parallel. For instance, the well-defined BP interface has a 3.7° angle between the basal planes from the matrix/twin and the prismatic planes from the twin/matrix for {10$\bar{1}$2} twins in Mg. We use simulated overlapping diffraction patterns for each zone axis to help visualize the planes in the matrix and twin that are nearly parallel and likely candidates to form interfaces. Some diffraction spots from the matrix and twin nearly overlap, indicating that the planes are nearly parallel. Only these nearly parallel planes are likely to form interfaces between the matrix and twin. We labeled likely planes in the simulated overlapping diffraction patterns and analyzed the angles between the two planes, allowing us to predict potential facets. Second, we combined different methods of identifying the edge-on facets in the HRTEM images depending on the observation zone axis. These include diffraction contrast, the mirror symmetry relationship between matrix and twin planes across the twin boundary, geometric phase analysis (GPA), phase contrast, and strain contrast. Diffraction contrast is a conventional TEM contrast mechanism often used at magnifications less than around 100,000× relying on the fact that the matrix and twin have different crystal orientations and,

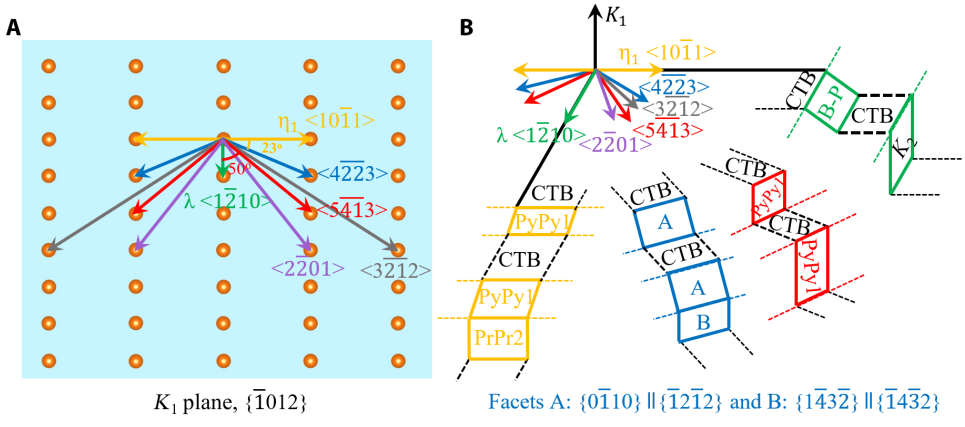

Fig. 1. Schematics of the atomic structure in K_1 plane and the facets in {$\bar{1}$012} twin boundaries. (**A**) Atomic configuration in the {$\bar{1}$012} twinning plane and low-index crystallographic directions. (**B**) Schematic of the facets identified from {$\bar{1}$012} twins observed by HRTEM from the six low-index crystallographic directions indicated in (A) and (B). A 3D twin domain of arbitrary shape could be built by combining the basic elements of CTBs and these facets in different length/height ratios.

thus, diffract electrons differently for most imaging conditions. A consequence of the twin orientation relationship is that a family of planes viewed down a zone axis contained within the K_1 plane exhibit mirror symmetry with respect to the K_1 plane. For most, but not all, of the zone axis contained within the K_1 plane, the twin boundary can be determined on the basis of the change in orientation of the planes across the twin boundary. All of the previous studies of twin facets from the <11$\bar{2}$0> relied on this characteristic of twin boundaries to define the boundary plane. GPA is normally used to measure in-plane displacements and/or strains at the nanometer scale within an HRTEM field of view using a fast Fourier transform (FFT)–based analysis of local lattice parameters (*31*, *32*). We use GPA in this study to measure small magnitude plane reorientations at the twin boundary for the <5$\bar{4}$$\bar{1}$3> zone axis. The <10$\bar{1}$1> zone axis represents a special case where the mirror image of the families of planes in the matrix exactly aligns with the same planes in the matrix, and thus, the boundary position cannot be determined based on a mirror symmetry relationship. However, the atoms within the interface are at slightly different positions relative to the parent and twin lattices, and the interface plane is often evident due to the resulting HRTEM phase contrast. Details of the methods used for determining boundary positions for each zone axis are given in the following content.

{$\bar{1}$012} twins facets viewed from <1$\bar{2}$10> zone axes

The facets of twin boundaries as viewed from <1$\bar{2}$10> are well established. For completeness, our observations from this direction are shown in Fig. 2 and fig. S1 for both extended twin boundaries (Fig. 2B) and twin tips (Fig. 2, C and D, and fig. S1). The simulated overlapping diffraction patterns in Fig. 2A show the BP/PB and K_2/K_2 planes to be closely aligned and likely candidates for facets. Our observations of CTBs, BP/PB facets, and K_2/K_2 facets from this direction are consistent with the ones reported in the literature (*8*, *11*, *16*, *25*–*29*). CTBs and BP/PB facets are generally easily distinguishable from this zone axis using the mirror symmetry relationship of planes across the boundary, because basal planes in the matrix are at approximately 84° to the basal planes in the twin. Figure 2D shows the atomic structure of a BP facet with dislocations labeled in the boundary. On the basis of the atomic structure, we studied the formation and stability of long BP facets in Mg in a recent paper (*33*).

{$\bar{1}$012} twin facets viewed from <5$\bar{4}$$\bar{1}$3> zone axes

The <5$\bar{4}$$\bar{1}$3> directions are 50° away from the <1$\bar{2}$10> direction. For the <5$\bar{4}$$\bar{1}$3> zone axis, the simulated overlapping diffraction patterns shown in Fig. 3A indicate that there are several pairs of nearly aligned planes in the parent and twin that may form interfaces, such as the pairs of spots labeled within the squares, ovals, and rectangles. The first three possible interfaces (ordered by d-spacing) are {0$\bar{1}$1$\bar{1}$} ‖ {01$\bar{1}$1} with a 4.8° angle (square symbols), {$\bar{1}$103} ‖ {$\bar{1}\bar{1}$21} with a 1.8° angle (oval symbols), and {$\bar{1}$2$\bar{3}$0} ‖ {$\bar{1}$2$\bar{1}$4} with a 3.4° angle (rectangular symbols).

Figure 3B shows the overall shape of a twin tip in an HRTEM micrograph viewed along a <5$\bar{4}$$\bar{1}$3> direction in the K_1 plane. The inset in Fig. 3B shows the selected-area electron diffraction (SAED) pattern from both the matrix and twin. The {01$\bar{1}$1} planes have the largest d-spacing among planes in the <5$\bar{4}$$\bar{1}$3> zone axis and can be observed in the enlarged HRTEM image shown in Fig. 3D. The (0$\bar{1}$1$\bar{1}$) planes of the matrix are 4.8° away from the (01$\bar{1}$1) planes of the twin. Because the angle is small between these planes, it is difficult

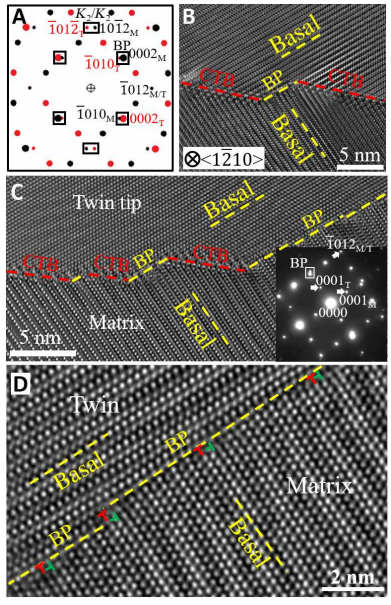

Fig. 2. Simulated diffraction patterns and images from {$\bar{1}$012} twins viewed along a <1$\bar{2}$10> zone axis within a K_1 plane. (**A**) Simulated overlapping diffraction patterns from twin (red dots) and matrix (black dots). (**B**) HRTEM image from an extended twin boundary containing CTBs and a BP facet. (**C**) HRTEM image from twin tip containing CTBs and BP facets. The inset is the selected-area electron diffraction (SAED) pattern from both the matrix and twin. (**D**) HRTEM image of a BP facet showing the atomic structure of the facet. The dislocations in the interface are labeled by dislocation symbols.

to discern the exact position of the boundary plane based solely on the mirror plane relationship. We combine FFT analysis, GPA analysis, and dislocation analysis to decipher where the twin boundaries lie. For the twin tip in Fig. 3B, FFT analysis was performed on the tip area (shown in fig. S2). The areas with only one set of diffraction spots (squares 1 and 3 in fig. S2A) correspond to either matrix or twin. The area with both diffraction spots (square 2 in fig. S2A) shows an overlap of matrix and twin spots at the boundary. Therefore, the rough position of the twin boundary is identified as within square 2. Second, GPA was performed in the vicinity of the twin tip. The result is shown in Fig. 3C overlapped with the corresponding HRTEM image. The colored map shows the relative rotation of {0$\bar{1}$1$\bar{1}$} planes from twin to matrix. The matrix is in yellow/red colors and the twin is in green/red colors that indicate that the interface is at the center of the square in Fig. 3C, which is enlarged in Fig. 3D. Figure 3D shows the rotation (4.8°) between the {0$\bar{1}$1$\bar{1}$} planes of matrix and {01$\bar{1}$1} planes of the twin; thus, the position where the two {0$\bar{1}$1$\bar{1}$} planes from twin to matrix meet can be identified. The dislocations necessary to accommodate the rotation at the boundary are labeled in Fig. 3D. The interface is indicated by black dashed lines and is identified as a pyramidal-(0$\bar{1}$1$\bar{1}$)$_M$ ‖ pyramidal-(01$\bar{1}$1)$_T$ (PyPy1) interface. MD simulations in what follows predict the existence of the PyPy1 facets and support this experimental result.

An HRTEM image from an extended twin boundary is shown in Fig. 3E. It shows a step along the CTB, which is also shown in the inset without lines for clearer observation purposes. The GPA result shown in Fig. 3F shows the relative rotation of {0$\bar{1}$1$\bar{1}$} planes from twin to matrix. The colored map also shows the step along the CTB. The facet at the step in the extended boundary is identified as a

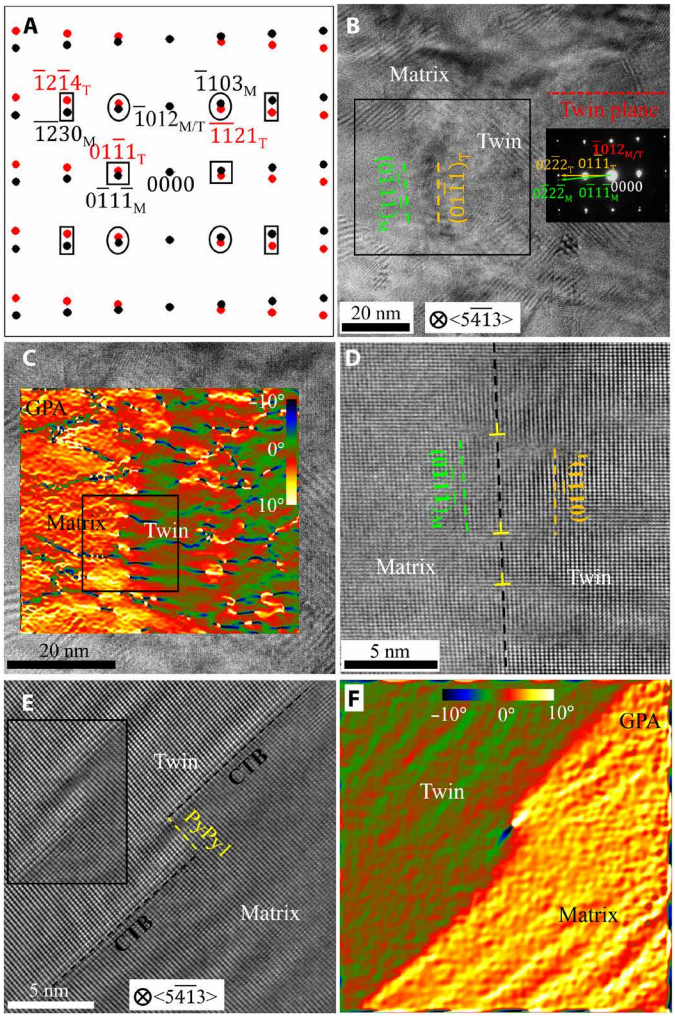

Fig. 3. Simulated diffraction patterns and images from {$\bar{1}$012} twins viewed along a <5$\bar{4}\bar{1}$3> zone axis within a K_1 plane. (**A**) Simulated overlapping diffraction patterns from twin (red dots) and matrix (black dots). (**B**) Relatively low-magnification HRTEM image from a twin tip showing the overall shape of the twin tip boundaries. The inset is the SAED pattern from both the matrix and twin. (**C**) GPA result for the square area in (B) overlapped with the corresponding HRTEM image, showing the relative rotation of {0$\bar{1}$1$\bar{1}$} planes from twin to matrix. (**D**) Enlarged HRTEM image of the square area in (C) with the interface and accommodating dislocations labeled in the image. (**E**) HRTEM image from an extended twin boundary containing CTBs and PyPy1 facet. (**F**) GPA result for the image in (E), showing the relative rotation of {0$\bar{1}$1$\bar{1}$} planes from twin to matrix.

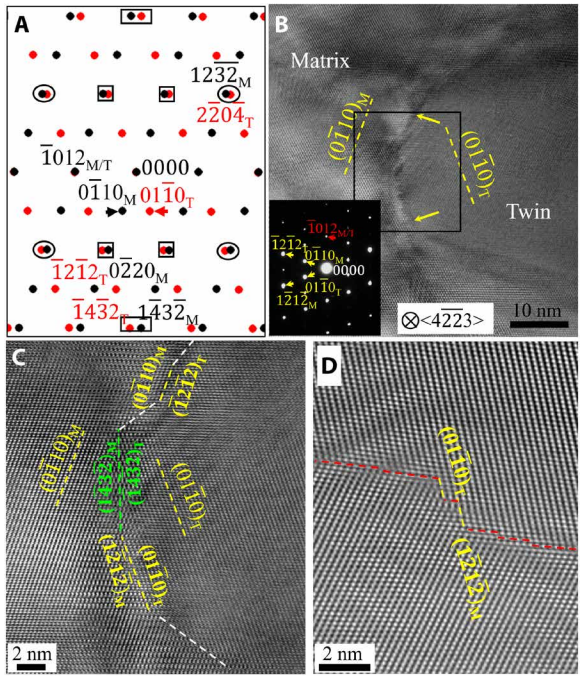

Fig. 4. Simulated diffraction patterns and images from {$\bar{1}$012} twins viewed along a <4$\bar{2}\bar{2}$3> zone axis within a K_1 plane. (**A**) Simulated overlapping diffraction patterns from twin (red dots) and matrix (black dots). (**B**) Relatively low-magnification HRTEM image from a twin tip showing the overall shape of the twin tip boundaries. The inset is the SAED pattern from both the matrix and twin. (**C**) Enlarged HRTEM image of the square area in (B) showing the {0$\bar{1}$10}‖{$\bar{1}$2$\bar{1}$2} and {1$\bar{4}\bar{3}\bar{2}$}‖{$\bar{1}$4$\bar{3}$2} facets. (**D**) HRTEM image from an extended twin boundary containing CTB and {0$\bar{1}$10}‖{$\bar{1}$2$\bar{1}$2} facets.

PyPy1 facet. Similar short steps were observed in other extended boundaries from this zone axis, and the facets observed in extended boundaries are much shorter than the facets observed in twin tips. The possible {$\bar{1}$103}‖{$\bar{1}\bar{1}$21} and {$\bar{1}$230}‖{$\bar{1}$2$\bar{1}$4} interfaces were not observed in either the twin tip or the extended twin boundary.

{$\bar{1}$012} twin facets viewed from <4$\bar{2}\bar{2}$3> zone axes

The <4$\bar{2}\bar{2}$3> directions are 67° away from the <1$\bar{2}$10> direction. The simulated overlapping diffraction patterns for a <4$\bar{2}\bar{2}$3> zone axis shown in Fig. 4A indicate that there are several pairs of nearly aligned planes in the parent and twin that may form interfaces, such as the pairs of spots labeled with squares, ovals, and rectangles. The first three possible interfaces (as ordered by d-spacing of the planes) are {0$\bar{1}$10}‖{$\bar{1}$2$\bar{1}$2} with a 2.5° angle (square signs), {12$\bar{3}\bar{2}$}‖{1$\bar{1}\bar{0}$2} with a 1.2° angle (oval signs), and {1$\bar{4}\bar{3}\bar{2}$}‖{$\bar{1}$4$\bar{3}$2} with a 2.8° angle (rectangular signs).

An HRTEM image from a twin tip is shown in Fig. 4B with an inset of the corresponding SAED pattern. Figure 4B shows the overall shape of the twin boundary, and it is obvious that the boundary between the two yellow arrows has sharp contrast, while the boundary beyond this segment is unidentifiable. The boundary between the two yellow arrows is enlarged and shown in Fig. 4C to show the atomic configuration. Planes with the largest d-spacing in the <4$\bar{2}\bar{2}$3> zone axis are {0$\bar{1}$10} planes, which are observed in Fig. 4C. There is a 40.0° angle between the (0$\bar{1}$10) planes in the matrix and the (01$\bar{1}$0) planes in the twin. We extend the two sets of {0$\bar{1}$10} planes from matrix and twin to the boundary and then identify the interface where these sets meet. The interfaces can be identified as {0$\bar{1}$10}‖{$\bar{1}$2$\bar{1}$2} and {1$\bar{4}\bar{3}\bar{2}$}‖{$\bar{1}$4$\bar{3}$2}, which are indicated by yellow and red dashed lines (the identification details are shown in fig. S3B). Interfaces indicated by white dashed lines are not identifiable. Figure 4D shows an HRTEM image from an extended twin boundary, and the same method was used to identify the facets along the twin boundary, as shown in fig. S3C. The facets along the extended twin boundary are confirmed as {0$\bar{1}$10}‖{$\bar{1}$2$\bar{1}$2}. However, the {0$\bar{1}$10}‖{$\bar{1}$2$\bar{1}$2} facets in the extended twin boundaries are shorter than that in the twin tip, which is similar to what was observed for the <5$\bar{4}\bar{1}$3> zone axis. The {1$\bar{4}\bar{3}\bar{2}$}‖{$\bar{1}$4$\bar{3}$2} facets have not been observed in extended twin

boundaries, and the possible $\{12\bar{3}\bar{2}\} \| \{1\bar{1}0\bar{2}\}$ interface was not observed in either the twin tip or the extended twin boundary.

{$\bar{1}$012} twin facets viewed from <10$\bar{1}$1> zone axes

As was previously stated, the orientation of a {$\bar{1}$012} twin is related to the orientation of the parent crystal by a 180° rotation about the <10$\bar{1}$1> shear direction. The diffraction spots from the matrix (black dots) and twin (red dots) in the <10$\bar{1}$1> shear direction exactly overlap, as shown in the simulated overlapping diffraction patterns of Fig. 5A. Because the diffraction patterns of the twin and matrix exactly overlap, there are many parallel planes, the first three of which (as ordered by d-spacing) are $(\bar{1}101)_M \| (0\bar{1}11)_T$, $(01\bar{1}\bar{1})_M \| (1\bar{1}0\bar{1})_T$, and $(\bar{1}2\bar{1}0)_M \| (1\bar{2}10)_T$.

Figure 5B shows a low-magnification image of a {$\bar{1}$012} twin viewed slightly off of the <10$\bar{1}$1> shear direction. The boundaries are observed in the low-magnification image due to diffraction contrast. The SAED pattern from the matrix and twin is inserted in Fig. 5B. The HRTEM image shown in Fig. 5C is obtained by zooming in on the extended twin boundary indicated in Fig. 5B. Because the mirror plane relationship of the K_1 plane for the <10$\bar{1}$1> zone axis results in the planes in the matrix perfectly aligning with the planes in the twin, this cannot be used to define the position of the twin boundary. In addition, the GPA analysis of Fig. 5C does not show any systematic in-plane strains associated with the twin boundary that can be used to define the boundary. While this is not helpful for distinguishing the atomic position of the boundary, it does confirm that the twin boundary defects viewed along the shear direction do not have significant edge character. However, Fig. 5C shows the position of the CTBs and a step separating them. The bright spots within the boundary are due to HRTEM phase contrast. The positions of the atoms that lie within the boundary twin are shifted slightly relative to the lattice positions within the parent and twin. This is obvious from the atomistic simulations shown in fig. S4. This slight difference in atomic column alignment when viewed down the <10$\bar{1}$1> direction results in a difference in HRTEM phase contrast. An enlarged image of the step is inset in Fig. 5C. The image in the square of Fig. 5C is enlarged and shown in Fig. 5D. The groups of {$\bar{1}$101} planes in matrix and twin are labeled by yellow and red dashed lines in Fig. 5D. The facet is identified as pyramidal-$(\bar{1}101)_M \|$ pyramidal-$(0\bar{1}11)_T$ (PyPy1) indicated by the yellow dashed line. The red dashed lines indicate CTBs.

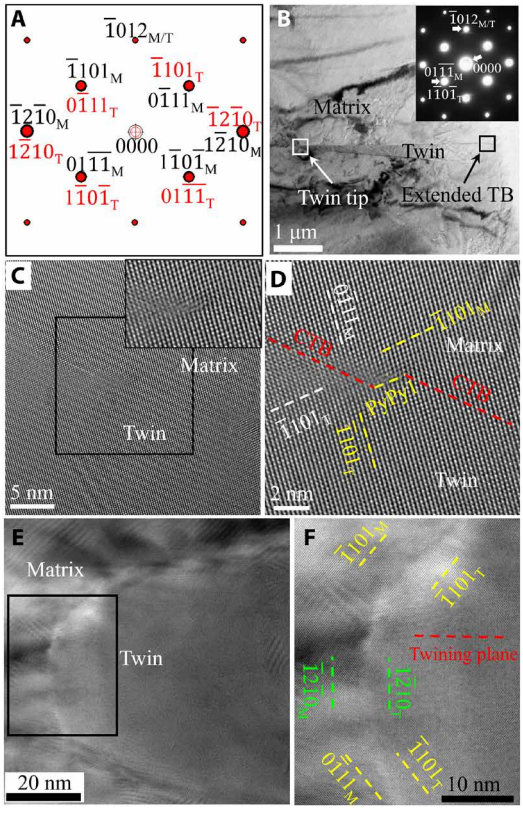

Fig. 5. Simulated diffraction patterns and images from a {$\bar{1}$012} twin viewed along the <10$\bar{1}$1> shear direction. (**A**) Simulated overlapping diffraction patterns; all diffraction spots from the twin (red dots) overlap with the spots from the matrix (black dots). (**B**) Low-magnification image showing the twin boundaries by diffraction contrast. The inset is the SAED pattern from both the matrix and twin. (**C**) HRTEM image from the extended twin boundary indicated in (B); the inset enlarges the image of the step along the CTB. (**D**) Enlarged image of the square area in (C), showing the CTBs and PyPy1 facet at the step. (**E**) Relative low-magnification HRTEM image from a twin tip indicated in (B) showing the overall shape of the twin tip boundaries. (**F**) Enlarged image of rectangle area in (E), showing the PyPy1 and possible PrPr2 facets.

Figure 5E shows an HRTEM image from the twin tip shown in the low-magnification image of Fig. 5B, viewed along the <10$\bar{1}$1> shear direction. It shows the overall shape of the twin tip. The boundaries inside the rectangle exhibit contrast and are enlarged in Fig. 5F, while the boundary outside the rectangle is unidentifiable. In Fig. 5F, there is sufficient contrast to suggest that some of the boundaries are consistent with the PyPy1 facets identified from the extended twin boundary shown in Fig. 5D. In addition, there is a long portion of the twin boundary at the tip that is roughly perpendicular to the twin K_1 plane. According to the simulated overlapping diffraction patterns, it is likely a prismatic-$(\bar{1}2\bar{1}0)_M \|$ prismatic-$(1\bar{2}10)_T$ (PrPr2) interface, which is perpendicular to the CTB. Moreover, a PrPr2 facet is predicted in the MD simulation shown in Fig. 6F, the same as independent MD simulations reported by Liu *et al.* (*30*). The evidence above leads us to believe that the twin tip contains both PyPy1 and PrPr2 facets.

MD characterization of {$\bar{1}$012} twin interfaces

We summarize the facets defining {$\bar{1}$012} twin boundaries determined by HRTEM in Fig. 1 and Table 1. In what follows, we use MD simulations for two purposes: (i) to substantiate the 3D atomistic configuration of the facets revealed by the essentially 2D sectioning process and (ii) to lay the ground work for future atomistic studies of the mobility of these facets. Unless agreement between measured and predicted equilibrium facets is achieved, one cannot take the next step consisting in dynamic propagation simulations. Because the crux of this work is to understand 3D properties of twin boundaries, it is necessary that the atomistic simulations used to support the HRTEM work be fully 3D.

To this end, a 3D twin domain is introduced into an atomistic domain representing the parent crystal. Figure 6A shows the initial twin structure at 100 K. A 1-GPa resolved shear stress is imposed on the twin system to grow the twin domain while maintaining the temperature of the overall domain at 100 K. Details of the MD construction and simulation are described in Materials and Methods and in the Supplementary Materials. As shown in Fig. 6A′, the 3D twin grows and develops faceted surfaces. All of the experimentally observed facets shown in Fig. 1B and listed in Table 1 are observed

in this simulation, with the exception of $\{1\bar{4}\bar{3}2\} \parallel \{\bar{1}4\bar{3}2\}$. In the simulation, CTBs become the largest interfaces through propagation of existing TDs. When viewed along the $[1\bar{2}10]$ direction, BP/PB and K_2 facets (delineated by solid red lines in Fig. 6B) are the second largest facets observed, which is consistent with the TEM images in Fig. 2 and fig. S1. Viewed along the $[5\bar{4}\bar{1}3]$ direction, $\{01\bar{1}1\} \parallel \{0\bar{1}1\bar{1}\}$ facets (delineated by red solid lines in Fig. 6C) are observed. The corresponding facets observed in the experiments are highlighted by yellow dashed lines in Fig. 3A. The black dashed lines in Fig. 6 (C to E) indicate boundaries with discrete TDs. When viewed along the $[4\bar{2}\bar{2}3]$ direction, small $\{0\bar{1}10\} \parallel \{\bar{1}2\bar{1}2\}$ facets (colored green in Fig. 6A′) are observed, consistent with the cross-section view normal to the $[4\bar{2}\bar{2}3]$ direction in Fig. 6D (delineated by red solid lines). In Fig. 6D, a small vertical segment along the trace of the $\{1\bar{4}\bar{3}2\} \parallel \{\bar{1}4\bar{3}2\}$ interface on the cross section is circled. However, this short segment is not the small facet depicted by green dashed line in Fig. 4A but the projection of $\{01\bar{1}1\} \parallel \{0\bar{1}1\bar{1}\}$ facets along the $[4\bar{2}\bar{2}3]$ direction, as can be inferred when comparing to the 3D configuration in Fig. 6A′. The comparatively small size of $\{1\bar{4}\bar{3}2\} \parallel \{\bar{1}4\bar{3}2\}$ experimental facets in Fig. 3A suggests a relatively high formation energy of this interface, and the MD simulation may not capture the feature. When viewed along the $[10\bar{1}1]$ direction, as shown in Fig. 6E, PyPy1 facets and small PrPr2 facets are observed, in agreement with the experimental observation in Fig. 5A.

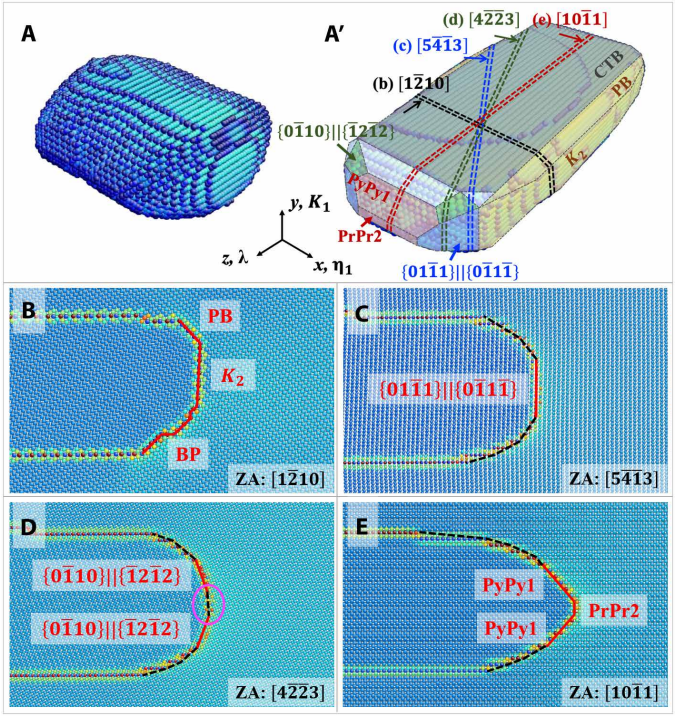

Fig. 6. MD characterization of {$\bar{1}$012} twin interfaces. (**A**) The 18 nm × 8 nm × 17 nm initial structure of the 3D ($\bar{1}$012) twin without stress relaxation of facets. (**A′**) The 21 nm × 8 nm × 41 nm final structure of the 3D ($\bar{1}$012) twin under 1-GPa shear stress associated with twinning at 100 K but without stress relaxation of facets. Cross-section view of twin tips/facets with (**B**) [1$\bar{2}$10], (**C**) [5$\bar{4}\bar{1}$3], (**D**) [4$\bar{2}\bar{2}$3], and (**E**) [10$\bar{1}$1] crystallographic directions. ZA, zone axis.

CONCLUSIONS

For twins to accommodate substantial deformation, the associated shear transformation must involve a non-negligible volume fraction of the grain, given by the relation $f^{twin} = \Delta\gamma^{twin}/S$, where $\Delta\gamma^{twin}$ is the amount of shear contributed by the twin system in the grain volume and S is the characteristic crystallographic shear ($S = 0.13$ for Mg). As a consequence, the twin domain not only must grow in thickness and propagate forward in the shear direction but also needs to expand laterally. The growth process is controlled by the formation energy and mobility of the 3D twin facets discovered here. MD allows one to address the kinetics evolution during twin growth, and our results indicate that this process is strongly anisotropic. The overall agreement between the predicted and the experimentally observed twin facets suggests that MD provides a viable path to predict and rationalize observed 3D microstructures.

The 3D twin configuration revealed by this work suggests the following conclusions and avenues for future exploration of 3D twin properties. An experimentally based description of the 3D configuration of twin boundaries is of fundamental importance for understanding the basic, atomic-scale mechanisms of deformation twinning. For instance, the simulations here indicate that twin propagation is not symmetric: Twins propagate faster in the $[1\bar{2}10]$ lateral direction relative to the "forward" $[10\bar{1}1]$ shear direction. This may be due to several combined factors: different mobilities of screw and edge

Table 1. Facets identified in 3D {$\bar{1}$012} twin domains and the corresponding observation directions.

Observation directions	Angle between observation directions and <1$\bar{2}$10>	Facets	Angle between facet and CTB
<1$\bar{2}$10>	0°	BP/PB	137°
		K_2/K_2	86°
<5$\bar{4}\bar{1}$3>	50°	PyPy1, $\{0\bar{1}1\bar{1}\} \parallel \{01\bar{1}1\}$	90°
<4$\bar{2}\bar{2}$3>	67°	$\{0\bar{1}10\} \parallel \{\bar{1}2\bar{1}2\}$	110°
		$\{1\bar{4}\bar{3}2\} \parallel \{\bar{1}4\bar{3}2\}$	89°
<10$\bar{1}$1>	90°	PyPy1, $\{\bar{1}101\} \parallel \{0\bar{1}11\}$	130°
		PrPr2, $\{\bar{1}2\bar{1}0\} \parallel \{1\bar{2}10\}$	90°

components of TDs, the relative differences in facet size along the different directions, and drag effects induced by the facet intersection zones of the twin domain. The overall shape of the twin, wider along the lateral dimension than along the propagation direction, is consistent with experimental EBSD observations reported by Liu *et al.* (*34*). On the basis of the current work, future studies of the effects of facet energies, mobilities, facet interactions with TDs or other facets, local stress fields, and solute segregation on facets will determine the factors affecting twin propagation and growth.

MATERIALS AND METHODS

Sample preparation and HRTEM

To perform HRTEM simultaneously in a twin and its parent, the viewing direction of both crystals must be along a low-index crystallographic direction or zone axis, i.e., a crystal direction that is perpendicular to multiple low-index crystal planes. For compound twins (all hcp twins) (*7*), this condition is only automatically satisfied for all low-index crystallographic directions that lie within the K_1 twinning plane. Specimens were prepared to obtain TEM foils with a distribution of foil normal directions near these special crystallographic directions.

Compression samples with dimensions of 8 mm × 9 × mm 10 mm were cut from a commercially pure, fully recrystallized polycrystal Mg plate, with the basal (0001) plane normal of most grains being within approximately 30° of the plate through thickness (TT) direction (8 mm). These cuboidal samples were compressed to a total engineering strain of 1.3% along the 10-mm direction, approximately perpendicular to the basal pole for most grains, resulting in twinning activity in most grains. For these grain orientations and compression direction, most activated $\{\bar{1}012\}$ twins are oriented at roughly ±45° to the compression and TT directions. The compressed samples were cut into ~1.2-mm-thick slices in two orientations. For the first orientation, the foil normal is perpendicular to the compression and TT directions such that zone axes within 45° of the λ $<11\bar{2}0>$ are accessible for many twins. For the second orientation, the foil normal is around 45° to the compression and TT directions such that zone axes within 45° of the η_1 $<10\bar{1}1>$ are accessible for many twins. The slices were thinned to 150 μm thick using 10% nitric acid and punched into 3-mm-diameter discs using a Gatan TEM sample punch. The 3-mm discs were electropolished to perforation in a solution of 2% nitric acid and water, a voltage of 0.1 V, and temperature of 2°C. Twin orientations and tips of interest were preselected using EBSD in an FEI Apreo scanning electron microscope. TEM and HRTEM investigations were conducted on an FEI Titan TEM with an imaging aberration corrector and an accelerating voltage of 300 kV. Images were captured on a Gatan OneView camera and analyzed using the Gatan Microscopy Suite (GMS 3). The GPA was performed in GMS 3 using the GPA plug-in from HREM Research Inc.

Atomic simulations

MD simulations were carried out using large-scale atomic/molecular massively parallel simulator (LAMMPS) (*35*). The simulations use the modified embedded-atom method (MEAM) potential developed for magnesium by Wu *et al.* (*36*). A 3D twin nucleus can be created following the pure-shuffle mechanism of $\{\bar{1}012\}$ twinning (*37*, *38*). Figure S5A shows the coherent dichromatic pattern associated with pure-shuffle nucleation of a $\{\bar{1}012\}$ twin. As shown in fig. S5B, the strained coherent dichromatic pattern is obtained by removing the mismatch strain between the BP plane in the matrix and the PB plane in the twin. Four types of shuffle vectors are defined in fig. S5B to move atoms in the matrix to their corresponding position in the twin. The construction of the simulation model starts with a 60 nm × 30 nm × 60 nm single crystal, with the x axis along the $[10\bar{1}1]$ direction, y axis normal to the $(\bar{1}012)$ plane, and z axis along the $[1\bar{2}10]$ direction. As shown in fig. S5C, a 6 nm × 6 nm × 12 nm nucleus bounded by PB, BP, and PrPr2 interfaces is first created, and the shuffle vectors are applied to atoms in the corresponding regions. Imposing periodic boundary conditions in the x and z directions and a 1-nm-wide fixed region on the y boundary, a relaxed twin structure as shown in fig. S5D is obtained at 5 K with multiple loading-unloading cycles under a deformation gradient with one nonzero simple shear component F_{12}. With the same boundary conditions, the temperature of the overall domain is brought to (and maintained at) 100 K and a 1-GPa resolved shear stress is imposed such as to trigger growth of the twin domain. The growth of the twin is shown in movie S1. The twin mainly propagates along the $[1\bar{2}10]$ direction and develops into a structure consisting of multiple facets.

SUPPLEMENTARY MATERIALS

Supplementary material for this article is available at http://advances.sciencemag.org/cgi/content/full/6/28/eaaz2600/DC1

REFERENCES AND NOTES

1. P. G. Partridge, The crystallography and deformation modes of hexagonal close-packed metals. *Metall. Rev.* **12**, 169–194 (1967).
2. M. R. Barnett, Twinning and the ductility of magnesium alloys: Part I: "Tension" twins. *Mater. Sci. Eng. A* **464**, 1–7 (2007).
3. L. Wu, A. Jain, D. W. Brown, G. M. Stoica, S. R. Agnew, B. Clausen, D. E. Fielden, P. K. Liaw, Twinning–detwinning behavior during the strain-controlled low-cycle fatigue testing of a wrought magnesium alloy, ZK60A. *Acta Mater.* **56**, 688–695 (2008).
4. S. J. Wang, T. Jozaghi, I. Karaman, R. Arroyave, Y. I. Chumlyakov, Hierarchical evolution and thermal stability of microstructure with deformation twins in 316 stainless steel. *Mater. Sci. Eng. A* **694**, 121–131 (2017).
5. S. Vercammen, B. Blanpain, B. C. De Cooman, P. Wollants, Cold rolling behaviour of an austenitic Fe–30Mn–3Al–3Si TWIP-steel: The importance of deformation twinning. *Acta Mater.* **52**, 2005–2012 (2004).
6. S. Wang, M. L. Sui, Y. T. Chen, Q. H. Lu, E. Ma, X. Y. Pei, Q. Z. Li, H. B. Hu, Microstructural fingerprints of phase transitions in shock-loaded iron. *Sci. Rep.* **3**, 1086 (2013).
7. J. W. Christian, S. Mahajan, Deformation twinning. *Prog. Mater. Sci.* **39**, 1–157 (1995).
8. B. Xu, L. Capolungo, D. Rodney, On the importance of prismatic/basal interfaces in the growth of $(\bar{1}012)$ twins in hexagonal close packed crystals. *Scr. Mater.* **68**, 901–904 (2013).
9. M. Gong, J. P. Hirth, Y. Liu, Y. Shen, J. Wang, Interface structures and twinning mechanisms of $\{\bar{1}012\}$ twins in hexagonal metals. *Mater. Res. Lett.* **5**, 449–464 (2017).
10. A. Luque, M. Ghazisaeidi, W. Curtin, Deformation modes in magnesium (0 0 0 1) and (0 1 $\bar{1}$ 1) single crystals: Simulations versus experiments. *Model. Simul. Mater. Sci. Eng.* **21**, 045010 (2013).
11. J. Wang, L. Liu, C. N. Tomé, S. X. Mao, S. K. Gong, Twinning and detwinning via glide and climb of twinning dislocations along serrated coherent twin boundaries in hexagonal-close-packed metals. *Mater. Res. Lett.* **1**, 81–88 (2013).
12. D. E. Spearot, L. Capolungo, C. N. Tomé, Shear-driven motion of Mg $\{10\bar{1}2\}$ twin boundaries via disconnection terrace nucleation, growth, and coalescence. *Phys. Rev. Mater.* **3**, 053606 (2019).
13. E. Martínez, L. Capolungo, C. N. Tomé, Atomistic analysis of the $\{10\bar{1}2\}$ twin stability and growth in α-Ti. *Phys. Rev. Mater.* **2**, 083603 (2018).
14. A. Luque, M. Ghazisaeidi, W. A. Curtin, A new mechanism for twin growth in Mg alloys. *Acta Mater.* **81**, 442–456 (2014).
15. J. P. Hirth, J. Wang, C. N. Tomé, Disconnections and other defects associated with twin interfaces. *Prog. Mater. Sci.* **83**, 417–471 (2016).
16. A. Ostapovets, A. Serra, Characterization of the matrix–twin interface of a $(10\bar{1}2)$ twin during growth. *Philos. Mag.* **94**, 2827–2839 (2014).
17. J. F. Nie, Y. Zhu, J. Liu, X.-Y. Fang, Periodic segregation of solute atoms in fully coherent twin boundaries. *Science* **340**, 957–960 (2013).

18. A. Kumar, J. Wang, C. N. Tomé, First-principles study of energy and atomic solubility of twinning-associated boundaries in hexagonal metals. *Acta Mater.* **85**, 144–154 (2015).
19. M. Ghazisaeidi, L. Hector Jr., W. Curtin, Solute strengthening of twinning dislocations in Mg alloys. *Acta Mater.* **80**, 278–287 (2014).
20. H. M. Zbib, M. Rhee, J. P. Hirth, On plastic deformation and the dynamics of 3D dislocations. *Int. J. Mech. Sci.* **40**, 113–127 (1998).
21. J. S. Barnard, J. Sharp, J. R. Tong, P. A. Midgley, High-resolution three-dimensional imaging of dislocations. *Science* **313**, 319 (2006).
22. B. P. Eftink, G. T. Gray, S. A. Maloy, Stereographic methods for 3D characterization of dislocations. *Microsc. Microanal.* **23**, 210–211 (2017).
23. N. Bertin, L. Capolungo, A FFT-based formulation for discrete dislocation dynamics in heterogeneous media. *J. Comput. Phys.* **355**, 366–384 (2018).
24. X. Y. Zhang, B. Li, X. L. Wu, Y. T. Zhu, Q. Ma, Q. Liu, P. T. Wang, M. F. Horstemeyer, Twin boundaries showing very large deviations from the twinning plane. *Scr. Mater.* **67**, 862–865 (2012).
25. B. M. Morrow, E. K. Cerreta, R. J. McCabe, C. N. Tomé, Toward understanding twin–twin interactions in hcp metals: Utilizing multiscale techniques to characterize deformation mechanisms in magnesium. *Mater. Sci. Eng. A* **613**, 365–371 (2014).
26. B. M. Morrow, R. J. McCabe, E. K. Cerreta, C. N. Tomé, Observations of the atomic structure of tensile and compressive twin boundaries and twin–twin interactions in zirconium. *Metall. Mater. Trans. A* **45**, 5891–5897 (2014).
27. T. Braisaz, P. Ruterana, G. Nouet, Twin tip defects related to the nucleation and growth mechanisms of the twin ($10\bar{1}2$) in zinc characterized by high-resolution electron microscopy. *Philos. Mag. A* **76**, 63–84 (1997).
28. Q. Sun, X. Y. Zhang, Y. Ren, J. Tu, Q. Liu, Interfacial structure of $\{10\bar{1}2\}$ twin tip in deformed magnesium alloy. *Scr. Mater.* **90**, 41–44 (2014).
29. J. Tu, X. Y. Zhang, Z. M. Zhou, C. Huang, Structural characterization of $\{10\bar{1}2\}$ twin tip in deformed magnesium alloy. *Mater Charact.* **110**, 39–43 (2015).
30. Y. Liu, N. Li, S. Shao, M. Gong, J. Wang, R. J. McCabe, Y. Jiang, C. N. Tomé, Characterizing the boundary lateral to the shear direction of deformation twins in magnesium. *Nat. Commun.* **7**, 11577 (2016).
31. F. Hüe, M. Hÿtch, H. Bender, F. Houdellier, A. Claverie, Direct mapping of strain in a strained silicon transistor by high-resolution electron microscopy. *Phys. Rev. Lett.* **100**, 156602 (2008).
32. M. Hÿtch, E. Snoeck, R. Kilaas, Quantitative measurement of displacement and strain fields from HREM micrographs. *Ultramicroscopy* **74**, 131–146 (1998).
33. K. Dang, S. Wang, M. Gong, R. J. McCabe, J. Wang, L. Capolungo, Formation and stability of long basal-prismatic facets in Mg. *Acta Mater.* **185**, 119–128 (2020).
34. Y. Liu, P. Z. Tang, M. Y. Gong, R. J. M. Cabe, J. Wang, C. N. Tomé, Three-dimensional character of the deformation twin in magnesium. *Nat. Commun.* **10**, 3308 (2019).
35. S. Plimpton, Fast parallel algorithms for short-range molecular dynamics. *J. Comput. Phys.* **117**, 1–19 (1995).
36. Z. Wu, M. F. Francis, W. A. Curtin, Magnesium interatomic potential for simulating plasticity and fracture phenomena. *Model. Simul. Mater. Sci. Eng.* **23**, 015004 (2015).
37. M. Gong, G. Liu, J. Wang, L. Capolungo, C. N. Tomé, Atomistic simulations of interaction between basal<a> dislocations and three-dimensional twins in Magnesium. *Acta Mater.* **155**, 187–198 (2018).
38. J. Wang, S. K. Yadav, J. P. Hirth, C. N. Tomé, I. J. Beyerlein, Pure-shuffle nucleation of deformation twins in hexagonal-close-packed metals. *Mater. Res. Lett.* **1**, 126–132 (2013).

Acknowledgments: We thank K. Dang for creating the supplementary atomistic simulation sections of a $\{\bar{1}012\}$ twin boundary showing the slightly shifted atoms at twin boundaries. **Funding:** This work is fully supported by the Office of Basic Energy Sciences, Project FWP 06SCPE401, under U.S. DOE contract no. W-7405-ENG-36. The electron microscopy was performed at the Electron Microscopy Lab at Los Alamos National Laboratory. **Author contributions:** S.W. performed the microscopy experiments. Atomistic simulations were conducted by M.G. and J.W. R.J.M., L.C., and C.N.T. conceived and coordinated the entire project. All authors contributed to the manuscript. **Competing interests:** The authors declare that they have no competing interests. **Data and materials availability:** All data needed to evaluate the conclusions in the paper are present in the paper and/or the Supplementary Materials. Additional data related to this paper may be requested from the authors.

Submitted 25 August 2019
Accepted 22 May 2020
Published 8 July 2020
10.1126/sciadv.aaz2600

Citation: S. Wang, M. Gong, R. J. McCabe, L. Capolungo, J. Wang, C. N. Tomé, Characteristic boundaries associated with three-dimensional twins in hexagonal metals. *Sci. Adv.* **6**, eaaz2600 (2020).